All-optical object identification and three-dimensional reconstruction based on computing metasurface

Dingyu Xu[1], Wenhao Xu[2], Qiang Yang[1], Wenshuai Zhang[1], Shuangchun Wen[1] and Hailu Luo[1]*

[1]Laboratory for Spin Photonics, School of Physics and Electronics, Hunan University, Changsha 410082, China; [2]School of Physics and Chemistry, Hunan First Normal University, Changsha 410205, China.

*Correspondence: hailuluo@hnu.edu.cn

This file includes:

Supplementary information for this paper is available at https://doi.org/10.29026/oea.2023.230120

Section 1: Theory of the optical computing metasurface produced light splitting
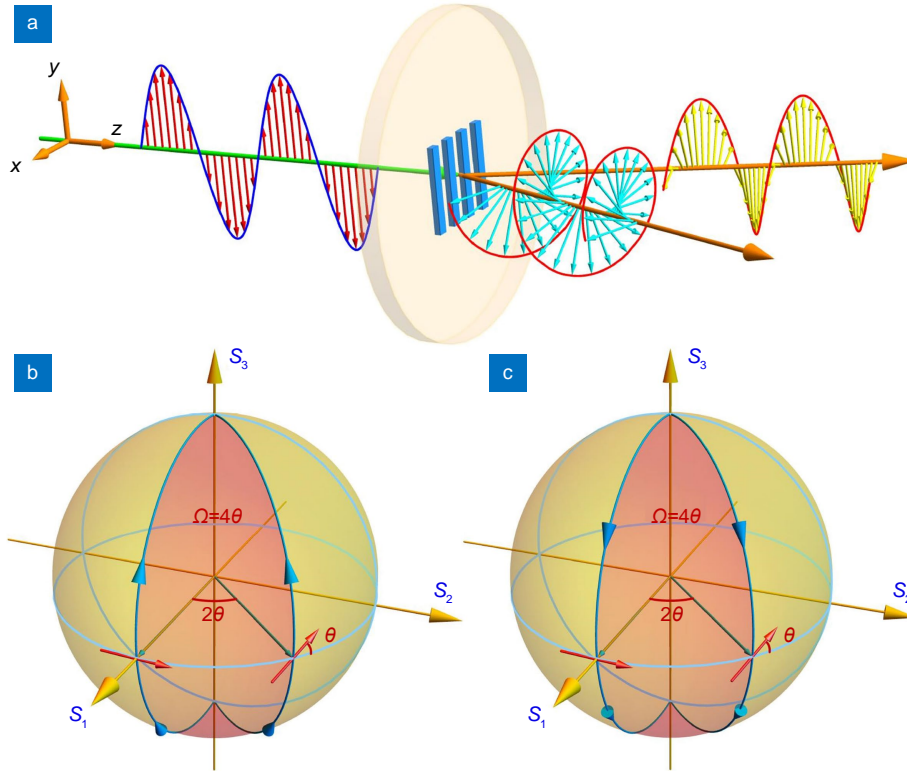

Fig. S1 | Scheme of the light transmission at the optical computing metasurface. (**a**) When the LP light beam impinges on the optical computing metasurface, the RCP and LCP light beam will be split with tiny displacements. (**b**) and (**c**) The RCP (LCP) light beam is converted into LCP (RCP) light beam with an additional geometric phase ±2θ in the three-dimensional Poincaré sphere, respectively.

The optical computing metasurface can be regarded as the half-wave plate with locally varying optical axis directions and uniform phase retardation because the operational wavelength is much larger than the characteristic dimension of the optical computing metasurface structures. Therefore, the Jones matrix of the optical computing metasurface can be given by

$$\boldsymbol{M}_{J} = \boldsymbol{r}\left(-\theta\right) \cdot \Delta\left(\pi\right) \cdot \boldsymbol{r}\left(\theta\right) = \begin{bmatrix} \cos2\theta & \sin2\theta \\ \sin2\theta & -\cos2\theta \end{bmatrix}, \tag{S1}$$

where $r\left(\theta\right)$ refers to the rotation matrix, $\theta\left(x\right) = \pi x/\Gamma$ represents the optical axis angle of the optical computing metasurface, Γ is the period of the phase gradient along the axis direction and $\Delta\left(\pi\right)$ is the phase retardation of the Jones matrix representations. When the linearly polarized light beam (LP) impinges on this metasurface, the left- (LCP) and right-circularly polarized (RCP) components would obtain the same displacements 2θ in opposite directions, which is shown in Fig. S1(a). This process can be written as follows [Fig. S1(b, c)]

$$\begin{aligned} \boldsymbol{E}_{\mathrm{opL}} &= \boldsymbol{M}_{J}\boldsymbol{L} = \exp\left(2\mathrm{i}\theta\right)\boldsymbol{R} \ , \\ \boldsymbol{E}_{\mathrm{opR}} &= \boldsymbol{M}_{J}\boldsymbol{R} = \exp\left(-2\mathrm{i}\theta\right)\boldsymbol{L} \ , \end{aligned} \tag{S2}$$

here $\boldsymbol{L} = 1/\sqrt{2}\begin{bmatrix} 1 & \mathrm{i} \end{bmatrix}^{\mathrm{T}}$, $\boldsymbol{R} = 1/\sqrt{2}\begin{bmatrix} 1 & -\mathrm{i} \end{bmatrix}^{\mathrm{T}}$. These equations demonstrate that the LCP (RCP) light beam would change to RCP (LCP) light beam and acquire an extra phase related to the optical axis angle θ of the optical computing metasurface, the extra phase is called Pancharatnam–Berry phase, which can be illustrated by the three-dimensional Poincaré sphere. The LCP (RCP) light evolves into RCP (LCP) along different paths from the north (south) pole to the south (north) pole in Fig. S1(b-c). Then we calculate the angular spectrum of the light field distribution when the optical computing metasurface is set at the Fourier plane, which can be written as

$$\widetilde{\boldsymbol{E}}_{\mathrm{opL}}\left(k_x, k_y\right) = \mathbb{F}\left[\boldsymbol{E}_{\mathrm{ip}}\left(x, y\right)\exp\left(2\mathrm{i}\theta\right)\boldsymbol{R}\right] = \widetilde{\boldsymbol{E}}_{\mathrm{ip}}\left(k_x, k_y\right)\exp\left(2\mathrm{i}\theta\right)\boldsymbol{R} \ , \tag{S3}$$

where $\mathbb{F}$ represents the Fourier operation and $k_{x,y}$ is the coordinate at the Fourier space. The light field distribution of the RCP at the output plane can be given as the following:

$$
\begin{aligned}
\boldsymbol{E}_{\mathrm{opML}}(x,y) &= \mathbb{F}\left[\widetilde{\boldsymbol{E}}_{\mathrm{opL}}(k_x, k_y)\right] \\
&= \mathbb{F}\left\{\mathbb{F}\left[\widetilde{\boldsymbol{E}}_{\mathrm{ip}}(k_x, k_y)\exp(2\mathrm{i}\theta)\,\boldsymbol{R}\right]\right\} \\
&= \mathbb{F}\left[\widetilde{\boldsymbol{E}}_{\mathrm{ip}}(k_x, k_y)\right] * \delta(x - \delta_x)\,\boldsymbol{R} \\
&= \boldsymbol{E}_{\mathrm{ip}}\left[(x - \delta_x), y\right]\boldsymbol{R}\ ,
\end{aligned}
\tag{S4}
$$

where $*$ is the convolution operation in Eq. (S4). According to the above steps, the light field distribution of the LCP at the output plane can be written as

$$
\boldsymbol{E}_{\mathrm{opMR}}(x,y) = \boldsymbol{E}_{\mathrm{ip}}\left[(x + \delta_x), y\right]\boldsymbol{L}\ .
\tag{S5}
$$

As we know, the LP light beam consists of LCP and RCP light beams, as a result of which the output light field after passing through the optical computing metasurface can be obtained as

$$
\boldsymbol{E}_{\mathrm{opM}}(x,y) = \frac{1}{\sqrt{2}}\boldsymbol{E}_{\mathrm{ip}}(x + \delta_x, y)\boldsymbol{L} + \frac{1}{\sqrt{2}}\boldsymbol{E}_{\mathrm{ip}}(x - \delta_x, y)\boldsymbol{R}\ ,
\tag{S6}
$$

where $\delta_x = \lambda f/\Gamma$, λ is the wavelength of the light source, and f refers to the focal length of the lens in this expression. After propagation through the optical metasurface, the second GLP can filter out the useless light to obtain the contour information of the object. The Jones matrix of the second GLP is as follows[S1]

$$
\begin{aligned}
\boldsymbol{M}_{\mathrm{G}} &= \boldsymbol{R}(-\Psi)\begin{bmatrix} 1 & 0 \\ 0 & 0 \end{bmatrix}\boldsymbol{R}(\Psi) \\
&= \begin{bmatrix} \cos^2\Psi & \cos\Psi\sin\Psi \\ \cos\Psi\sin\Psi & \sin^2\Psi \end{bmatrix} = \begin{bmatrix} 0 & 0 \\ 0 & 1 \end{bmatrix}\ ,
\end{aligned}
\tag{S7}
$$

where Ψ equals $\pi/2$ in the current system. When the output field $\boldsymbol{E}_{\mathrm{opM}}(x,y)$ passes through the second GLP, the final output light field distribution in the whole differentiator system can be acquired as

$$
\begin{aligned}
\boldsymbol{E}_{\mathrm{op}}(x,y) &= \boldsymbol{M}_{\mathrm{G}} \cdot \boldsymbol{E}_{\mathrm{opM}}(x,y) \\
&= \frac{1}{2}\boldsymbol{E}_{\mathrm{ip}}(x + \delta_x, y)\begin{bmatrix} 0 \\ \mathrm{i} \end{bmatrix} + \frac{1}{2}\boldsymbol{E}_{\mathrm{ip}}(x - \delta_x, y)\begin{bmatrix} 0 \\ -\mathrm{i} \end{bmatrix} \\
&= \frac{1}{2}\left[\boldsymbol{E}_{\mathrm{ip}}(x + \delta_x, y) - \boldsymbol{E}_{\mathrm{ip}}(x - \delta_x, y)\right]\begin{bmatrix} 0 \\ \mathrm{i} \end{bmatrix}\ .
\end{aligned}
\tag{S8}
$$

Since the dimensions of objects are much more than the displacements δ_x in Eq. (S8), $\boldsymbol{E}_{\mathrm{op}}(x,y)$ can be approximately expressed as

$$
\boldsymbol{E}_{\mathrm{op}}(x,y) \approx \mathrm{i}\delta_x\frac{\partial \boldsymbol{E}_{\mathrm{ip}}(x,y)}{\partial x}\ .
\tag{S9}
$$

According to the expression $I_{\mathrm{op}}(x,y) = |\boldsymbol{E}_{\mathrm{op}}(x,y)|^2$, the light field intensity captured by the CCD can be written as

$$
I_{\mathrm{op}}(x,y) = \boldsymbol{E}_{\mathrm{op}}(x,y)\,\boldsymbol{E}_{\mathrm{op}}^*(x,y) \approx \left|\mathrm{i}\delta_x\frac{\partial \boldsymbol{E}_{\mathrm{ip}}(x,y)}{\partial x}\right|^2\ .
\tag{S10}
$$

Section 2: Fabrication of the optical computing metasurface

The optical computing metasurface can be considered as a half-wave plate with homogeneous phase retardation because the characteristic dimension of the optical computing metasurfaces nanostructures is much smaller than the wavelength, which can be written as

$$
\tau = \frac{2\pi D_s}{\lambda}(n_{\mathrm{E}} - n_{\mathrm{O}})\ ,
\tag{S11}
$$

where $(n_{\mathrm{E}} - n_{\mathrm{O}})$ is the induced birefringence, and $n_{\mathrm{E,O}}$ are extraordinary and ordinary refractive indices, respectively. D_s is the writing depth of the nanostructure, and λ is the working wavelength, the working wavelength employed in this

system being 632.8 nm. The expression of $n_{E,O}$ can be written as[S2]

$$n_E = \sqrt{\frac{(n_1 n_2)^2}{m n_2^2 + (1-m) n_1^2}} \,, \tag{S12}$$

$$n_O = \sqrt{m n_1^2 + (1-m) n_2^2} \,. \tag{S13}$$

where $n_{1,2}$ are the refractive indices of the two media that constitute the nanostructure of the optical computing metasurface, respectively. m is the duty cycle, it is 0.1−0.2. At the operation wavelength of 632.8 nm, $(n_E - n_O)$ approximately to $-(2-4) \times 10^3$, the etching depth is 80 μm, and the etching period is 8 mm.

Figure S2(a) exhibits the sample of the optical computing metasurface, the glass substrate is 25 mm-diameter, 3 mm-thickness, and the nanostructure area of the sample is 4 mm × 4 mm. Using the cross-polarization approach, the distribution of the partial optical slow-axis of the sample nanostructure has been demonstrated in Fig. S2(b), which clearly illustrates the gradient mode along the x axis. The scanning electron microscope (SEM) result in Fig. S2(c) reflects the size of the birefringent nanostructure is approximately on the order of 30 − 100 nm. The characteristic dimension of the nanostructure is far less than the operation wavelength in the experiment, thus, it can be considered a half-wave plate with homogeneous phase retardation. The detailed fabrication of the optical computing metasurface is completed by Altechna Co. Ltd. The preparation progress is described in previous research ref.[S2].
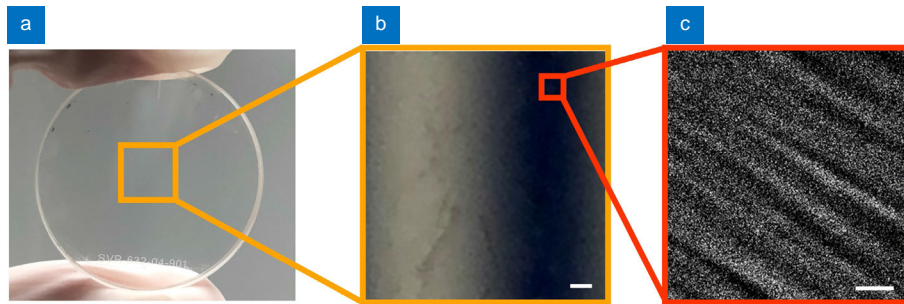

Fig. S2 | Fabrication of the optical computing metasurface. (**a**) Image of the optical computing metasurface embedded in 25 mm-diameter glass substrate, the area of the sample is 4 mm × 4 mm. (**b**) Cross polarization result of the sample in (a). Scale bar, 300 μm. (**c**) The SEM image of the nanostructure about the optical computing metasurface. Scale bar, 100 nm.
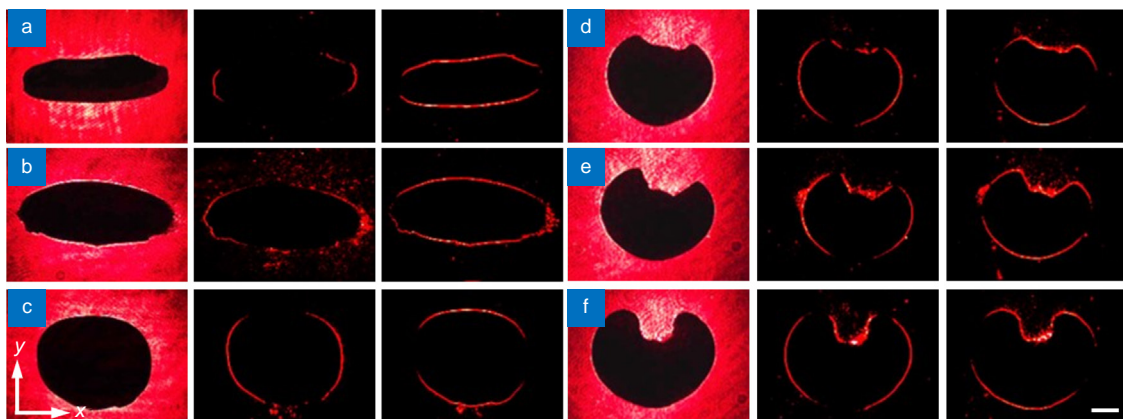

Fig. S3 | Results of object identification about the high-contrast object. (**a–c**) The experimental results of black rice, oats, and mung beans processed by the all-optical identification system, respectively. (**d–f**) The results of different forms of job's tears processed by the all-optical identification system, respectively. Scale bar, 1000 μm.

Section 3: Object identification experiments of high- and low-contrast objects

To distinguish different types of objects, the object identification system can also be used to inspect the appearance of different individuals in the same species. We now further demonstrate the object identification ability of the all-optical system that is important for imaging processing. For this purpose, high-contrast objects, such as black rice, oats, and

mung, bean have been chosen to exhibit the capability of this object identification system in Fig. S3(a–c). Three lines in Fig. S3(a–c) exhibit the ordinary images, as well as the contour surfaces along the *x* axis and *y* axis of black rice, oats, and mung bean, respectively. In addition to distinguishing different types of objects, the object identification system can also be used to inspect the appearance of different individuals in the same species. The job's tears have been used to illustrate the selection capability of object identification. The images of the job's tears without using the second GLP are represented in the first lines in Fig. S3(d–f), respectively. Other images in Fig. S3(d–f) display the contour information images after the second orthogonal GLP with two different orientations of the metasurface. The different shapes of the job's tears can be easily observed in the second and third lines in Fig. S3(d–f), especially the cupped parts in the middle, which might be beneficial for the research of the biological characters.

To further demonstrate the object identification ability of low-contrast objects, the experiment of different shapes of objects has been designed in this section. Figure S4(a) displays the image of a low-contrast object prepared by the photolithography method, and the etching patterns on it exhibit in Fig. S4(b), which includes letters, cats, moons, loving hearts, stars, and squares. Taking advantage of the same setups in Fig. 2(a), the contour information can be captured by a CCD camera. Letters "$\hbar$", "ϕ", "Ψ", "σ" in Fig. S4(c1–f2) have been used to verify the ability to distinguish different shapes of low-contrast objects, as well as the moon and "Schrödinger's Cat" patterns in Fig. S4(g1–j2) have been used for confirming the ability to identify different sizes of low-contrast objects. By extracting their contour information in the *x* and *y* direction, it can be found that objects with inconsistent shapes or sizes can be well recognized.
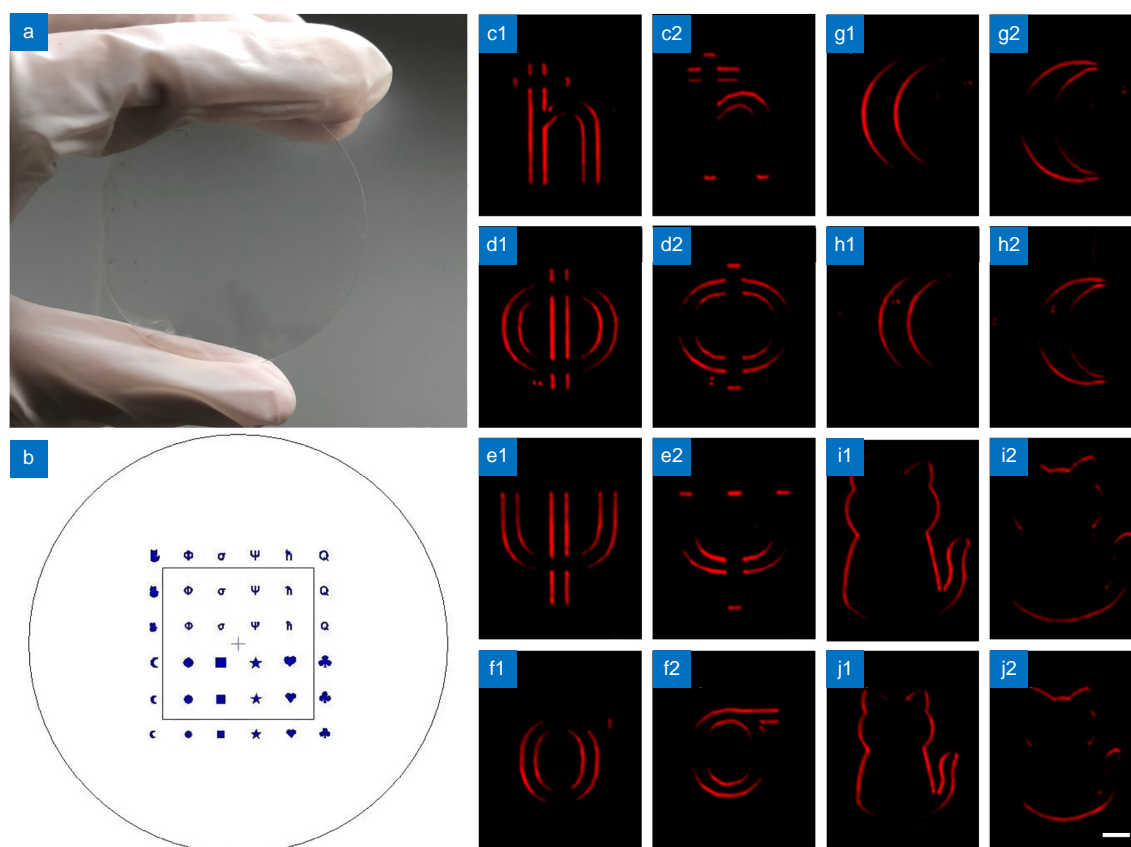

Fig. S4 | Results of object identification about the low-contrast object. (**a**) Image of the low-contrast object embedded in a similar circular glass substrate with a diameter of 50 mm, the area of the sample is 33 mm×33 mm. (**b**) The etching patterns of the low-contrast object. (**c1−f2**) Experiment results of different shapes of the low-contrast object processed by the proposed all-optical system. (**g1−j2**) The results of moon patterns and "Schrödinger's Cat" patterns with different sizes are acquired by the identification system, respectively. Scale bar, 500 μm.

Section 4: Calculation of low-contrast 3D object reconstruction process

To illustrate the principle of 3D reconstruction of low-contrast objects, a schematic diagram is shown in Fig. S5. For low-contrast 3D objects [$E_{\mathrm{ip}}(x, y) = \exp[\mathrm{i}\phi(x, y)]$], it's hard to directly measure their thickness with regular measuring
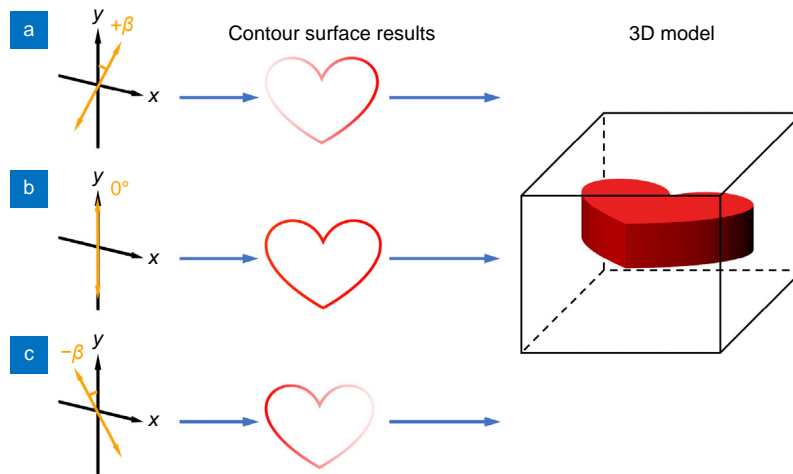
Fig. S5 | Scheme of 3D reconstruction about the low-contrast object. (a-c) The different contour surface results captured by rotating the optical axis of the second GLP with different angles $+\beta$, 0, and $-\beta$, respectively. Taking advantage of these three results, the 3D model can be reconstructed successfully.

tools. When they pass through this all-optical orthometric system [Fig. S5(b)], the output light field can be obtained as

$$\boldsymbol{E}_{\mathrm{op}}\left(x, y\right) = -\,\delta_x \exp\left[\mathrm{i}\boldsymbol{\phi}\left(x, y\right)\right] \frac{\partial \boldsymbol{\phi}\left(x, y\right)}{\partial x} \ . \tag{S14}$$

The measured intensity can be approximated as

$$I_{\mathrm{op}}\left(x, y\right) = \boldsymbol{E}_{\mathrm{op}}\left(x, y\right) \boldsymbol{E}_{\mathrm{op}}^{*}\left(x, y\right) = \left|-\delta_x \exp\left[\mathrm{i}\boldsymbol{\phi}\left(x, y\right)\right] \frac{\partial \boldsymbol{\phi}\left(x, y\right)}{\partial x}\right|^2 \ . \tag{S15}$$

According to Eq. (S15), it can be found that the current operation cannot distinguish the signs between the positive and negative phases. Therefore, in order to distinguish the sign of the phase, a bias has been introduced into the proposed 3D reconstruction system by rotating the second GLP with a tiny angle ($\pm\beta$). The transmission light field distribution can be rewritten as [Fig. S5(a) and S5(c)]

$$\boldsymbol{E}_{\mathrm{op}}^{\pm\beta}\left(x, y\right) = \exp\left[\mathrm{i}\boldsymbol{\phi}\left(x, y\right)\right]\left[-\delta_x \cos\beta \frac{\partial \boldsymbol{\phi}\left(x, y\right)}{\partial x} \mp \sin\beta\right] \ . \tag{S16}$$

Then the phase gradient can be obtained as

$$\nabla_{\boldsymbol{P}} = \frac{\partial \boldsymbol{\phi}\left(x, y\right)}{\partial x} = \frac{\sqrt{I_{\mathrm{op}}\left(x, y\right)}}{-\delta_x \exp\left[\mathrm{i}\boldsymbol{\phi}\left(x, y\right)\right]} \mathrm{sgn}\left(\left|\boldsymbol{E}_{\mathrm{op}}^{\beta}\left(x, y\right)\right|^2 - \left|\boldsymbol{E}_{\mathrm{op}}^{-\beta}\left(x, y\right)\right|^2\right) \ . \tag{S17}$$

Since the intensity of the low-contrast object has the expression $I\left(x, y\right) = \left|\exp\left[\mathrm{i}\boldsymbol{\phi}\left(x, y\right)\right]\right|^2 = 1$, Eq. (S17) can be further simplified as

$$\nabla_{\boldsymbol{P}} = \frac{\sqrt{I_{\mathrm{op}}\left(x, y\right)}}{-\delta_x} \mathrm{sgn}\left(\left|\boldsymbol{E}_{\mathrm{op}}^{\beta}\left(x, y\right)\right|^2 - \left|\boldsymbol{E}_{\mathrm{op}}^{-\beta}\left(x, y\right)\right|^2\right) \ . \tag{S18}$$

Here, the phase information of the low-contrast 3D object can be reconstructed by the captured results on the CCD. By subtracting two images carrying different phase information to obtain the signs of the phase [Eq. (S18)], then acquiring phase gradient results from the edge information by Eq. (S14). In order to recover the phase gradients to the phase information of the object, we combine the phase gradients in vector form $\nabla_{\boldsymbol{P}} = \left(\nabla_x \nabla_y\right)^{\mathrm{T}}$, and the expression between them contained in each pixel can be written as the following ref.[S3]

$$\boldsymbol{\phi}\left(x, y\right) = \boldsymbol{M}_{\mathrm{E}}^{-1}\boldsymbol{M}_{\mathrm{D}}\nabla_{\boldsymbol{P}}\boldsymbol{S} \ , \tag{S19}$$

where S is the size of each pixel, M_{D} and M_{E} are two sparse matrices related to pixels. Ultimately, making use of the least squares method could recover the initial phase $\boldsymbol{\phi}\left(x, y\right)$. The process of the whole calculation can be described in Fig. S5(a–c), we chose the rotation angle β as 1° in this experiment.

Since the representation of the equation between the phase retardation and thickness of the object can be described as[S1]

$$d = \frac{\lambda \phi(x, y)}{2\pi (n_{\mathrm{g}} - n_{\mathrm{a}})} \; , \tag{S20}$$

where $n_{\mathrm{g,a}}$ are the refractive index of the glass substrate and air, respectively, the all-optical 3D reconstruction of the low-contrast object can be achieved by the system we proposed. Therefore, this system can not only reconstruct the regular 3D object but also the low-contrast 3D object.

References

S1. Kasap SO. *Optoelectronics and Photonics* 2nd ed (Pearson, Boston, 2013).

S2. Beresna M, Gecevičius M, Kazansky PG. Polarization sensitive elements fabricated by femtosecond laser nanostructuring of glass. *Opt Mater Express* **1**, 783–795 (2011).

S3. Southwell WH. Wave-front estimation from wave-front slope measurements. *J Opt Soc Am* **70**, 998–1006 (1980).